ACS OMEGA

http://pubs.acs.org/journal/acsodf

Article

Density Functional Theory Study on the Enhancement Mechanism of the Photocatalytic Properties of the g-C_3N_4/BiOBr(001) Heterostructure

Wenzhi Yao, Dongying Li, Shuai Wei, Xiaoqing Liu, Xuefei Liu, and Wentao Wang*

Cite This: *ACS Omega* 2022, 7, 36479−36488

Read Online

ACCESS | Metrics & More | Article Recommendations | Supporting Information

ABSTRACT: The van der Waals heterostructures fabricated in two semiconductors are currently attracting considerable attention in various research fields. Our study uses density functional theory calculations within the Heyd−Scuseria−Ernzerhof hybrid functional to analyze the geometric structure and electronic structure of the g-C_3N_4/BiOBr(001) heterojunction in order to gain a better understanding of its photocatalytic properties. The calculated band alignments show that g-C_3N_4/BiOBr can function as a type-II heterojunction. In this heterojunction, the electrons and holes can effectively be separated at the interface. Moreover, we find that the electronic structure and band alignment of g-C_3N_4/BiOBr(001) can be tuned using external electric fields. It is also noteworthy that the optical absorption peak in the visible region is enhanced under the action of the electric field. The electric field may even improve the optical properties of the g-C_3N_4/BiOBr(001) heterostructure. Given the results of our calculations, it seems that g-C_3N_4/BiOBr(001) may be significantly superior to visible light photocatalysis.

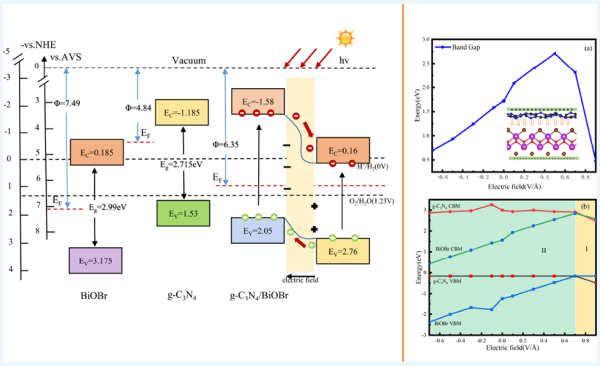

1. INTRODUCTION

The use of photocatalysis has recently attracted much attention due to its significant potential for applications such as solar energy utilization and the elimination of pollutant pollutants,[1−5] which is both green and efficient. The solar utilization efficiency of pure semiconductor photocatalysts such as TiO_2,[6,7] ZnO,[8] and $SrTiO_3$[9,10] is hampered by their wide band gap, which negatively impacts solar utilization. In spite of this, BiOBr possesses better photocatalytic oxidation and reduction activities due to its band gap, which is appropriate for visible light irradiation (∼2.8 eV).[11−14] The indirect transition band gap of BiOBr can reduce the probability of recombination between excited electrons and holes since the excited electrons must travel a certain distance across the *k*-space to be emitted into the valence band (VB) once excited.[15] Additionally, it possesses a highly anisotropic layered crystal structure with double Br^- layers and $[Bi_2O_2]^{2+}$ layers arranged alternately along the c-axis in a [−Br−Bi−O−O−Bi−Br−] arrangement. The layers are stacked on top of each other by the forces known as van der Waals (vdW) forces. Therefore, the BiOBr lamellar structure is relatively sparse, and the modified lamellar structure is readily dissociated along the direction (001).[16−18]

It has been demonstrated that graphitic carbon nitride (g-C_3N_4), investigated for hydrogen evolution and environmental purification under visible light, provides excellent photocatalysis capabilities due to its 2.7 eV band gap and high thermal and chemical stability.[19] However, pure g-C_3N_4 is limited by its poor light absorption and high recombination rate of photogenerated electron−hole pairs, which restricts its application as a visible light catalyst. There are numerous approaches to improving the efficiency of photocatalysis. Among these, the construction of heterojunction structures has been considered a powerful way to modify the atomic and electronic structures of photocatalysts to accelerate electron−hole separation and transport. During the formation of a heterojunction between g-C_3N_4, a potential difference is formed between the VB and the conduction band (CB) at the interface. When exposed to visible light (>400 nm) irradiation, electrons are easily excited in g-C_3N_4, and they can quickly form holes−electron pairs in this material. The photogenerated electrons are transferred to the CB of another semiconductor when the interaction between the potential differences occurs, thereby suppressing the recombination of photogenerated carriers. Therefore, g-C_3N_4-based heterojunctions have attracted extensive research interest since they are effective visible light catalysts.[20−27]

Received: July 7, 2022
Accepted: September 23, 2022
Published: October 4, 2022

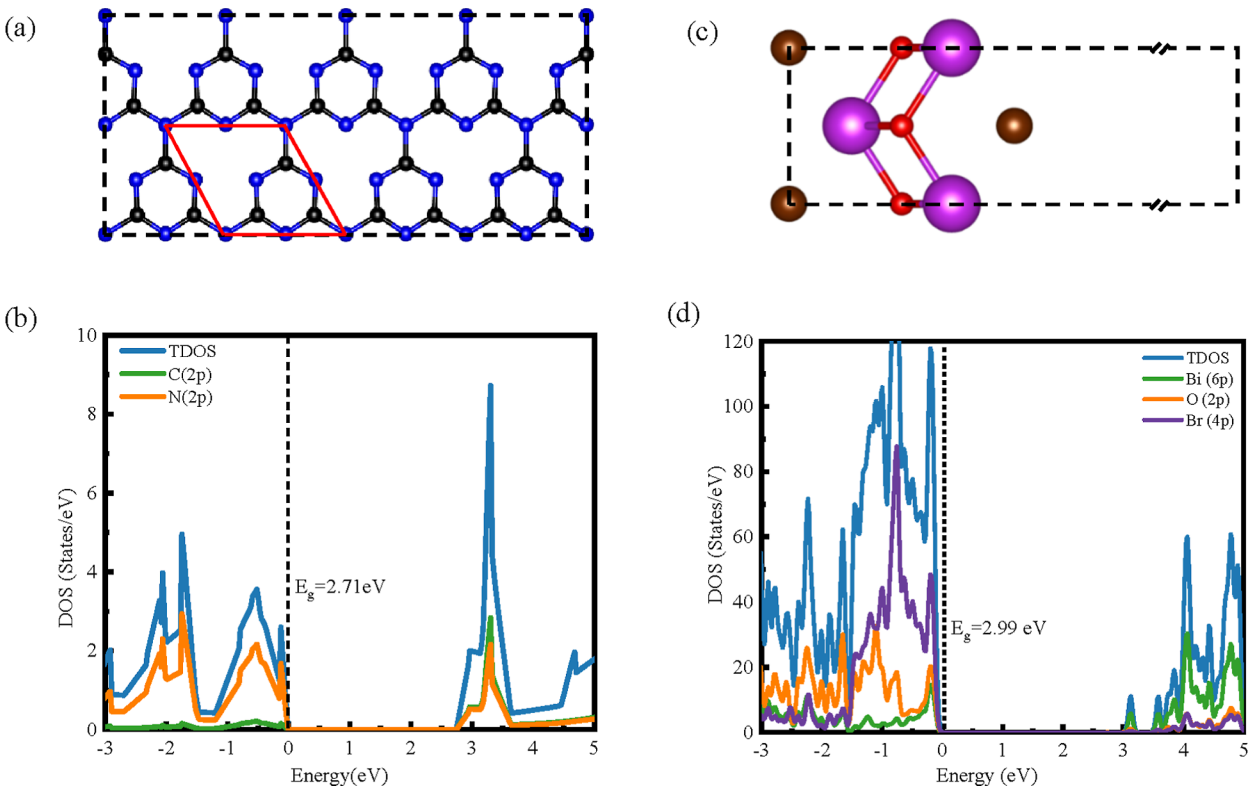

Figure 1. (a) Structure of the g-C_3N_4 monolayer. The red line shows the cell used for the calculation and the black and blue balls represent C and N atoms, respectively. (b) TDOS and PDOS of the g-C_3N_4 layer. (c) BiOBr(001) surface. The purple, red, and brown balls represent Bi, O, and Br atoms, respectively. (d) TDOS and the corresponding PDOS of the BiOBr(001) facet.

The g-C_3N_4 and BiOBr semiconductor bands are found to overlap in previous studies, and these results are expected to continue. It is believed that their energy levels are well-matched and suitable for making heterojunction catalysts that respond to visible light. The experiment demonstrated that the g-C_3N_4/BiOBr heterojunction had good photocatalytic activity for the photodegradation of organic contaminants (such as rhodamine B).[28−34] Nevertheless, the mechanisms for improving the photocatalytic performance of the suggested samples are different. Yan et al.[35] have found that the holes (h^+) in the VB of BiOBr could directly oxidize organic pollutants. According to Zhang et al.,[31] the composite interface created a powerful built-in electric field. Using the combined effects of band edge bending and Coulomb forces to form a BiOBr/g-C_3N_4 heterojunction with an S-type charge-transfer pathway, the researchers found that their system displayed significantly improved catalytic activity. Interestingly, Huang et al.[34] showed that the BiOBr/g-C_3N_4 photocatalyst enhanced the redox ability of the photogenerated electrons and holes through an indirect Z-scheme photocatalytic mechanism. This results in significantly increased photodegradation activity of rhodamine B, bisphenol A, and tetracycline under light-emitting diode illumination. However, the reason for the improved photocatalytic performance is still unclear. Therefore, the mechanism of improving the photocatalytic performance of BiOBr/g-C_3N_4 heterojunctions needs to be explored.

Our work here studies g-C_3N_4/BiOBr(001) using Heyd−Scuseria−Ernzerhof (HSE) hybrid density functional theory (DFT) calculations to understand its geometry, electronic structure, and photocatalytic properties. The calculated band alignments show that the g-C_3N_4/BiOBr can function as a type-II heterojunction. This heterojunction allows the electrons and holes to be separated at the interface. Moreover, we find that the electronic structure and band alignment of g-C_3N_4/BiOBr(001) can be tuned with external electric fields. It is also noteworthy that the optical absorption peak in the visible region is enhanced under the action of the electric field. The electric field may even improve the optical properties of the g-C_3N_4/BiOBr(001) heterostructure. Our results will further the understanding of the enhancement mechanism of the photocatalytic properties of the g-C_3N_4/BiOBr(001) heterostructure.

2. CALCULATION METHODS

In order to conduct the first-principles calculations, we used the Vienna ab initio simulation package (VASP)[36,37] along with the projector-augmented wave (PAW) method,[38] based on the DFT. In order to perform the structural relaxation and self-consistent calculations, the generalized gradient approximation (GGA),[39] based on the Perdew−Burke−Ernzerhof (PBE) functional, is employed.[40] It is also important to mention that since all band structures and optical properties are calculated based on HSE functionals,[41] 85% semi-local PBE exchange, and 15% exact non-local Hartree−Fock exchange, this method can avoid underestimating the band gaps in GGA-PBE calculations. Because standard PBE functionals do not describe the weak interactions well, an empirical correction scheme of the DFT-D3(BJ) method in the Grimme scheme is used for nontrivial vdW interactions.[42] A dipole correction[43] is employed to compensate for the dipole interactions. A kinetic energy cutoff of 550 eV is used, and a 1 × 3 × 1 Monkhorst−Pack *k*-point grid is used for the first Brillouin zone sampling. We relaxed all geometries to their full extent, and the energy

https://doi.org/10.1021/acsomega.2c04298
ACS Omega 2022, 7, 36479−36488

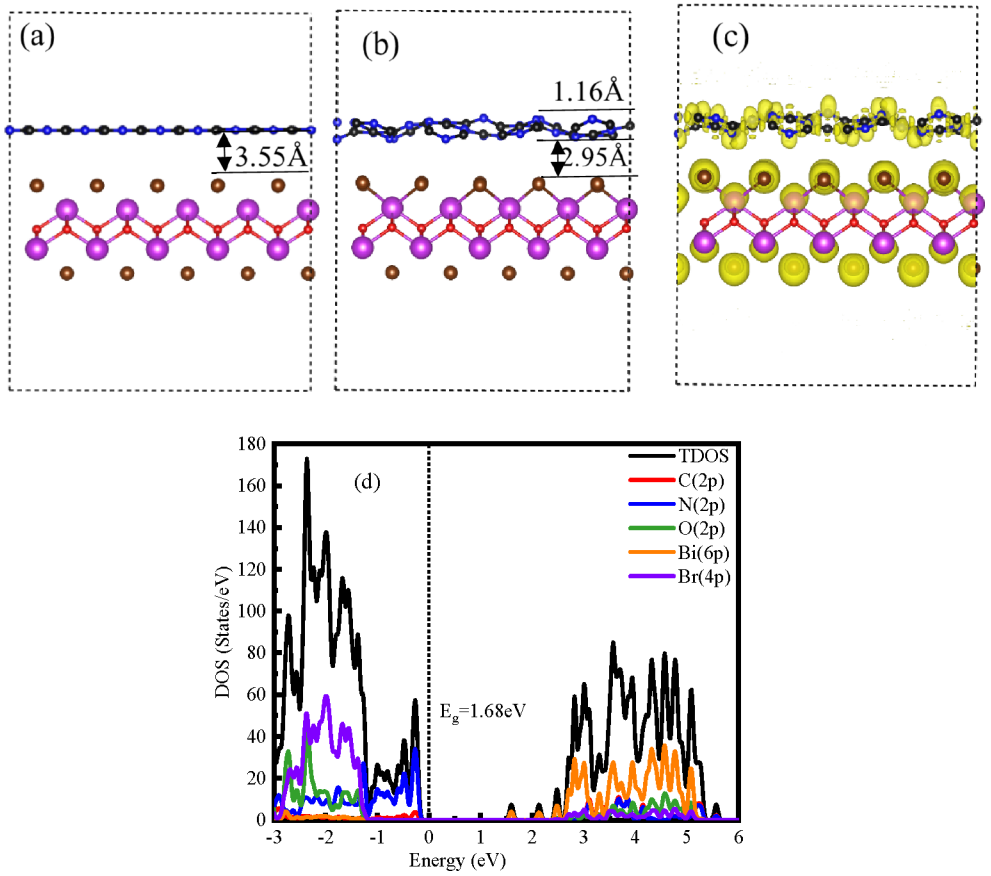

Figure 2. g-C_3N_4/BiOBr(001) heterojunction structure before (a) and after geometry optimization (b). (c) Electron localization function (ELF) and (d) TDOS and PDOS of the g-C_3N_4/BiOBr(001) vdW heterojunction. All the TDOS and PDOS are calculated by using the HSE06 function. The vertical lines indicate the Fermi levels.

convergence criteria are set to 10^{-4} eV and the force convergence criteria are set to 0.03 eV/Å. An additional vacuum spacing of 15 Å is added along the direction perpendicular to the 2D nanosheet to avoid interference and periodic impacts between neighboring layers. It is possible to use external electrostatic fields for slab calculations or molecular calculations based on manipulating the dipole moment in a slab. Adding an artificial dipole layer in the middle of the vacuum in the *z*-direction is performed to simulate the effect of the in-plane electric field.

3. RESULTS AND DISCUSSION

3.1. g-C_3N_4/BiOBr(001) Heterojunction. First, we investigated the structures of g-C_3N_4 and BiOBr(001) sequentially, as shown in Figure 1, before expounding upon the g-C_3N_4/BiOBr(001) heterojunction properties. By optimizing the original cells of g-C_3N_4 and BiOBr(001), we obtained the lattice constants of a = 4.74 Å for the g-C_3N_4 monolayer and a = 3.86 Å and c = 5.62 Å for the BiOBr(001) surface (Figure 1a,b). It has been shown that the Br-termination BiOBr(001) surface has a significantly lower surface energy than the BiO-terminated BiOBr(001) surface.[11] Hence it is highly likely to be integrated into ultrathin nanosheets (Note S1). Thus, in order to build ultrathin 2D hybridized-layered heterojunctions composed of g-C_3N_4/BiOBr(001), BiOBr(001) with Br termination is selected. We also perform the ab initio molecular dynamics (AIMD) simulations[44] at 300 K for 8 ps with 8000 time steps to test the thermal stability of g-C_3N_4/BiOBr(001) (Note S2).

To obtain more accurate electronic structure analysis results, we calculated the total density of states (TDOS) and partial density of states (PDOS) of g-C_3N_4 and BiOBr(001) using the HSE method, and the results are shown in Figure 1c,d, respectively. The calculated band gaps are 2.71 eV for the monolayer of g-C_3N_4 and 2.99 eV for the BiOBr(001) surface. Compared to the experimental and theoretical values of 2.78 and 2.94 eV, respectively, previously reported in the literature,[31] they are in good agreement. The computation method we have chosen is reasonably practical and feasible. Figure 1c,d show sthat the VB of g-C_3N_4 is occupied by N 2p, while the CB is made up of the hybridized C 2p and N 2p orbitals. While Br 4p mainly occupies the VB of BiOBr(001) and O 2p and Bi 6p orbitals, the CB is composed of the Bi 6p orbital track composition.

In this study, we present an ultrathin g-C_3N_4/BiOBr(001) heterojunction achieved by stacking g-C_3N_4 on top of BiOBr(001) in the vertical direction with the consideration of the vdW interactions. The 5 × 2 rectangular cells of BiOBr(001) with a dimension of 19.615 Å × 7.846 Å are employed, which can be matched with $2\sqrt{3} \times 1$ cells of the g-C_3N_4(001) monolayer. It resulted in a very small mismatch in the crystal's lattice structure (x-direction: 3.3%, y-direction: 4.7%). There are 116 atoms in a single cell (Figure 2a) in the g-C_3N_4/BiOBr(001) heterojunction. When the heterojunction structure is completely relaxed, the interaction between the g-

https://doi.org/10.1021/acsomega.2c04298
ACS Omega 2022, 7, 36479−36488

C_3N_4 monolayer and the BiOBr(001) surface results in g-C_3N_4 flakes with a slightly irregular shape (Figure 2b), and the interlayer distance remains the same at 2.95 Å, which is a vdW distance.[45−47] This can be further proved by the electron localization function (ELF), as shown in Figure 2c. The yellow area is one of the strongest sites of electron localization. We can see that the highest degree of electron localization is observed in the bonding region of monolayer BiOBr(001) and monolayer g-C_3N_4. Almost no electron localization is observed in the interface region, which clearly illustrates that g-C_3N_4/BiOBr(001) is subject to vdW interactions at the heterojunction interface, and no chemical bonds are formed there.

In order to evaluate the stability of the heterojunction as well as to characterize the interlayer interaction intensity, we calculated the interfacial adhesion energy [E(ab)] using the following equation[35]

$$E(\mathrm{ab}) = \{E(\mathrm{comb}) - E[\text{g-}C_3N_4] - E[\mathrm{BiOBr}(001)]\}/A \quad (1)$$

where E(comb), E[g-C_3N_4], and E[BiOBr(001)] denote the total energy of the relaxed g-C_3N_4/BiOBr(001), pristine g-C_3N_4 monolayer, and Br-terminated BiOBr(001) layer, respectively, and A denotes the surface area. A 0.14 eV/Å^2 correlation between g-C_3N_4 and the BiOBr(001) surface indicates that these interfaces are stable.

To investigate the possible reasons for the high photocatalytic activity of g-C_3N_4/BiOBr(001), we have examined its TDOS and PDOS, as shown in Figure 2d. The band gap of the g-C_3N_4/BiOBr(001) heterojunction is reduced to approximately 1.68 eV after forming the hybrid interface. This indicates an increase in the charge transfer efficiency from the VB to the CB of the g-C_3N_4/BiOBr(001) heterojunction. In Figure 2d, it is clearly shown that the valence band maximum (VBM) of g-C_3N_4/BiOBr(001) is primarily occupied by N 2p and C 2p orbitals, whereas Bi 6p orbitals occupy the conduction band minimum (CBM). In addition, additional evidence may be obtained from the decomposed charge densities of the CBM and VBM. As shown in Figure 3, the

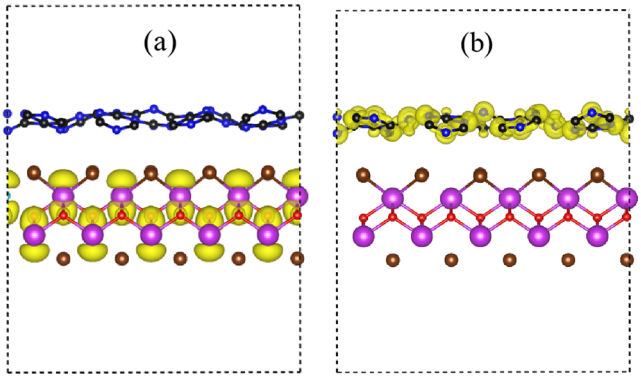

Figure 3. Partial charge density of the CBM (a) and the VBM (b) for the g-C_3N_4/BiOBr(001) heterojunction. The isosurface value is 0.0003 e/Å^3. The labeling of the atoms is the same as that in Figure 1.

VBM is derived from C and N atoms, while the CBM originates from Bi atoms, respectively. It has been found that the VBM of BiOBr(001) is lower than that of g-C_3N_4. In comparison, the CBM of g-C_3N_4 is higher than that of BiOBr(001). Based on the analysis above, we have found that the g-C_3N_4/BiOBr(001) heterojunction has a typical type-II energy band arrangement structure. The electron−hole pairs with the lowest energy will spontaneously separate in the type-II heterojunction. This means that the g-C_3N_4/BiOBr(001) heterojunction exhibits greater photoresponse to visible light than the g-C_3N_4 monolayer or pristine BiOBr(001).

The Fermi levels of g-C_3N_4, BiOBr(001), and g-C_3N_4/BiOBr(001) heterojunctions are −3.43, −3.34, and −1.25 eV, respectively. The Fermi level change significantly implies charge redistribution after g-C_3N_4 coupling to the BiOBr(001) surface. To further confirm this result, the planar average differential charge density of g-C_3N_4/BiOBr(001) is calculated according to the following formula[48]

$$\Delta\rho = \int \rho_{\mathrm{T}}(x, y, z)\mathrm{d}x\ \mathrm{d}y - \int \rho_{\mathrm{BiOBr}}(x, y, z)\mathrm{d}x\ \mathrm{d}y - \int \rho_{\text{g-}C_3N_4}(x, y, z)\mathrm{d}x\ \mathrm{d}y \quad (2)$$

where $\rho_{\mathrm{T}}(x,y,z)$, $\rho_{\mathrm{BiOBr}}(x,y,z)$, and $\rho_{\text{g-}C_3N_4}(x,y,z)$ represent the charge densities of the g-C_3N_4/BiOBr(001) heterojunction, BiOBr(001) surface, and g-C_3N_4 monolayer, respectively. According to this definition, the positive/negative values of $\Delta\rho$ represent charge accumulation/depletion, respectively. As shown in Figure 4, the $\Delta\rho$ distribution along the z-direction

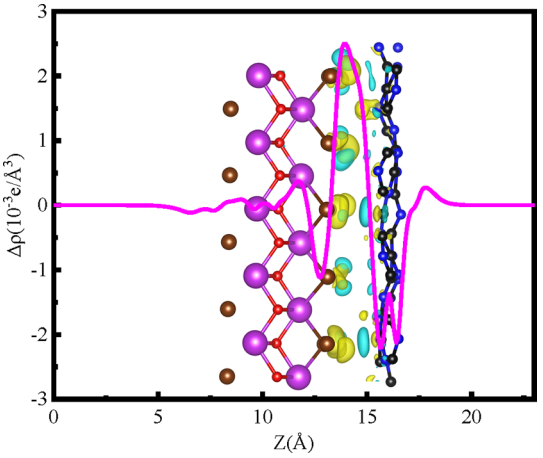

Figure 4. Planar-averaged differential charge density $\Delta\rho(z)$ and 3D charge density differences of the g-C_3N_4/BiOBr(001) heterojunction. The yellow and cyan regions represent charge accumulation and depletion, respectively, and the isosurface value is 0.0003 e/Å^3. The labeling of the atoms is the same as that in Figure 1.

(vertical to the interface) is shown. In this figure, the pink line indicates the change in charge density along the Z direction for the plane-averaged charge density difference along the Z direction. Electron accumulation occurs when the values are positive, while electrons are depleted when the values are negative. The charge density changes at the interface, indicating that electrons are transferred from the g-C_3N_4 side to the BiOBr(001) side, while holes remain in the g-C_3N_4 side. Moreover, we can clearly observe this transition from the 3D charge density difference between g-C_3N_4 and BiOBr(001). On the left side of Figure 4, the isosurface value represents a value of 0.0003 e/Å^3, and the yellow and cyan regions indicate the accumulation and depletion of charge, respectively. In addition, the Bader charge analysis[49] further confirmed the charge transfer from g-C_3N_4 to the BiOBr(001) slab. This analysis showed that 0.07e is transferred from g-C_3N_4 to the BiOBr(001) slab. A net charge accumulation at the interface

https://doi.org/10.1021/acsomega.2c04298
ACS Omega 2022, 7, 36479−36488

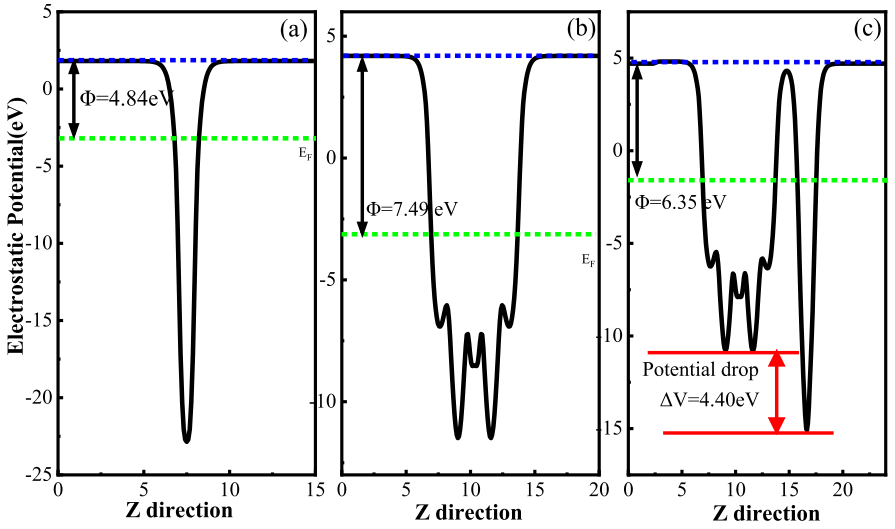

Figure 5. Work functions of (a) g-C_3N_4 monolayer, (b) BiOBr (001) surface, and (c) g-C_3N_4/BiOBr(001) heterojunction. The blue and green dashed lines represent the Fermi level and the vacuum energy level (E_0), respectively. Φ denotes the work function.

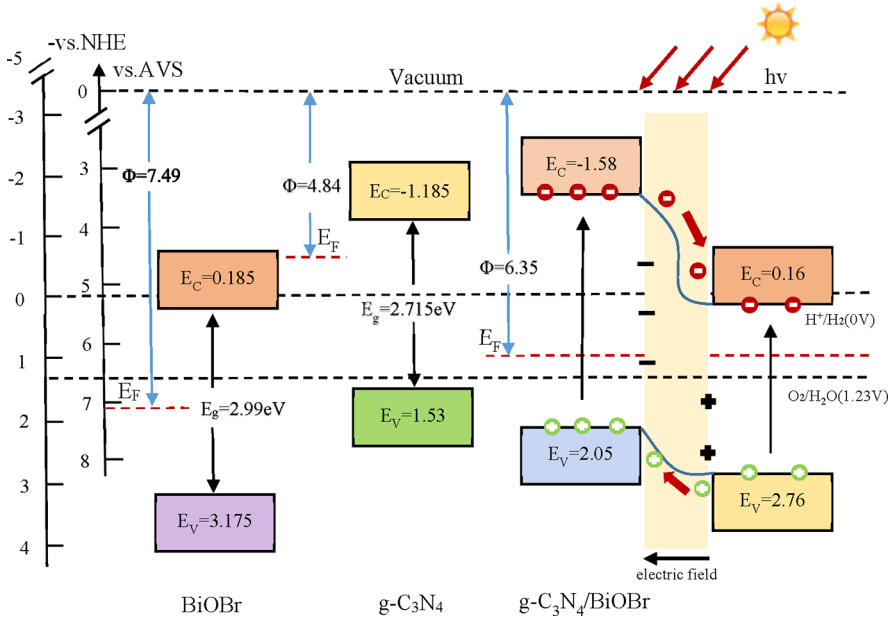

Figure 6. Schematic diagram of the energy band edge positions before and after the contact between g-C_3N_4 and BiOBr(001) and the charge separation at the interface of C_3N_4/BiOBr(001) under visible light irradiation, where Φ is the work function, E_C is the bottom of the CB, E_V is the top of the VB, and E_g is the band gap.

results in the formation of an electric field, favoring the separation of electrons from holes.

A band alignment is an essential indicator for studying heterojunctions and their practical applications. The work functions of g-C_3N_4, BiOBr(001), and g-C_3N_4/BiOBr(001) are calculated to understand this alignment process of the heterojunction better. The work function is defined as $\Phi = E_{vac} - E_F$, where E_{vac} denotes the energy of the stationary electron near the surface in a vacuum and E_F is the Fermi level.[50−52] The work functions of the g-C_3N_4 monolayer, the BiOBr(001) surface, and the g-C_3N_4/BiOBr(001) heterojunction are shown in Figure 5a−c. According to our calculations, the work functions of g-C_3N_4, the BiOBr(001) surface, and the g-C_3N_4/BiOBr(001) heterojunction are 4.63, 7.12, and 6.19 eV, respectively. There can be a significant potential drop (4.40 eV), resulting in the electron being driven from g-C_3N_4 to BiOBr(001), resulting in positively charged g-C_3N_4 and negatively charged BiOBr(001). A spontaneous interfacial charge transfer occurs when the g-C_3N_4 layer reaches equal Fermi levels with the BiOBr(001) layer, forming an internal electric field in the interface between the two layers. At the same time, the energy bands of g-C_3N_4 shift upward by 1.56 eV, while the energy bands of BiOBr shift downward by 0.93 eV along with their own Fermi level. Consequently, the CBM of BiOBr(001) increases, which is higher than that of g-C_3N_4. However, the VBM of g-C_3N_4 decreases, which is lower than that of BiOBr(001). These results agree with the previously discussed differences in charge density and the Bader charge analysis.

Figure 6 shows a schematic diagram of the energy band structures of g-C_3N_4 and BiOBr(001) before and after contact. To discuss the charge transfer at the interface and the energy

https://doi.org/10.1021/acsomega.2c04298
ACS Omega 2022, 7, 36479−36488

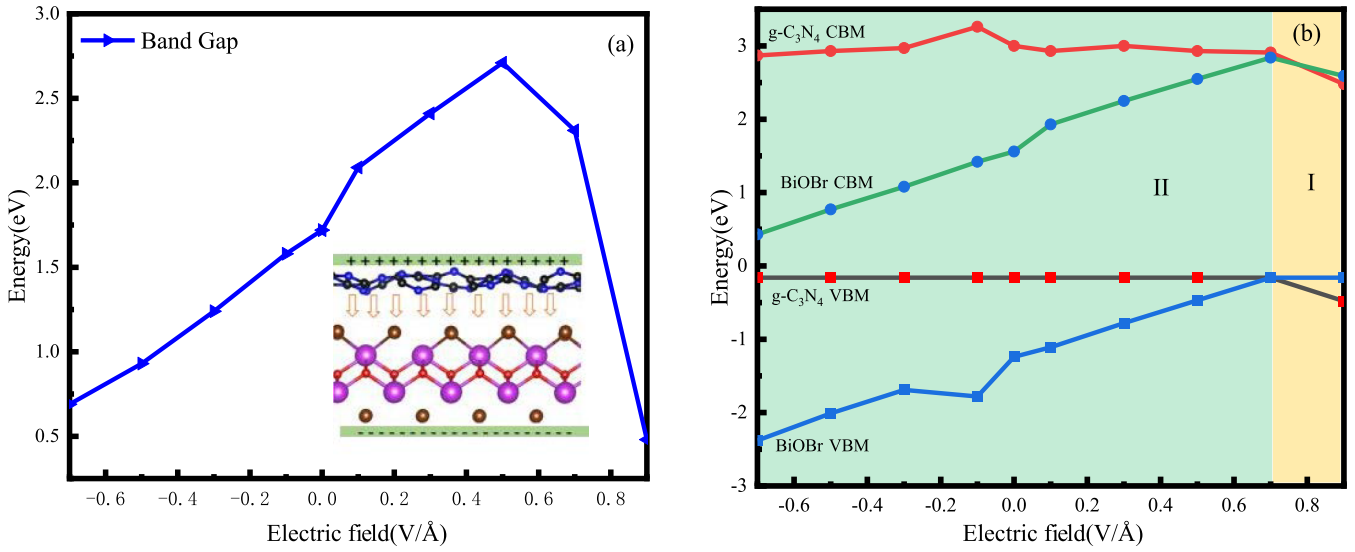

Figure 7. (a) Variation of the band gap with the electric field and (b) variation trend of the CBM and VBM of g-C_3N_4 and BiOBr with the electric field.

level matching between the separated two components, the band edge energies of the CB and VB of g-C_3N_4, the BiOBr(001) surface, and the g-C_3N_4/BiOBr(001) heterostructure are calculated according to the following equation[50]

$$E_{CB} = \chi - E_0 - 0.5E_g \quad (3)$$

$$E_{VB} = E_{CB} + E_g \quad (4)$$

where χ refers to the absolute electronegativity of the semiconductor and E_{CB}, E_{VB}, and E_g are the CB and VB edge potentials and the band gap of the semiconductor, respectively. E_0 is the scaling factor relating the redox level of the reference electrode to the absolute vacuum scale (AVS) [E_0 = 4.5 eV for the normal hydrogen electrode (NHE)]. The relationship between E_{NHE} and E_{AVS} is defined as $E_{AVS} = -E_{NHE} - E_e$. The χ values of g-C_3N_4 and BiOBr(001) are 4.67[53] and 6.18 eV,[54] respectively. The E_g values of g-C_3N_4 and BiOBr(001) sheets are 2.71 and 2.99 eV, respectively. According to 4, the CB and VB edge potentials of g-C_3N_4 are −1.19 and 1.53 eV, respectively, relative to the NHE. Furthermore, the CB and VB edge potentials of BiOBr(001) are 0.19 and 3.18 eV, respectively, relative to the NHE. As shown in Figure 6 (left), all the positions of the energy band edges for g-C_3N_4 and BiOBr(001) are calculated before contact. Under visible light irradiation, electrons are photoexcited from the VB to the CB for the g-C_3N_4 and BiOBr(001) layers. As shown in Figure 6 (right), the g-C_3N_4/BiOBr(001) heterojunction absorbs light energy, which excites electrons in the VB to the CB, thus causing holes to be left in the VB. Some photogenerated electrons generated by the g-C_3N_4 layer will continuously flow into the CB of BiOBr(001). At the same time, some photogenerated holes generated by BiOBr(001) will move to the VB of g-C_3N_4. This will result in the accumulation of holes at the VB of g-C_3N_4 and the accumulation of electrons at the CB of BiOBr(001). Due to this, the photogenerated e^- and h^+ are effectively separated into different surfaces by the built-in electric field. It is thought that spatial separation inhibits the recombination of e^-/h^+ and increases the lifetime of photogenerated carriers, thereby improving the quantum efficiency of photocatalysis.[55,56]

In order to evaluate the photocatalytic water splitting activity of g-C_3N_4/BiOBr(001), we compared the partitioned band edge potentials with the oxidation and reduction potentials of the g-C_3N_4 and BiOBr(001) layers. According to thermodynamic requirements, the decomposition of water can only occur when the CBM of the electronic structure is higher than the reduction potential of H^+/H_2 (0 V vs NHE at pH = 0). The VBM of the electronic structure is higher than the oxidation potential of O_2/H_2O (1.23 V vs NHE at pH = 0). It is found that before contact, the CBM and VBM potentials of BiOBr(001) are 0.19 eV higher than the reduction potential of H^+/H_2 and 1.9 eV higher than the oxidation potential of O_2/H_2O, respectively, indicating that the BiOBr(001) is only suitable for the oxygen evolution reaction (OER).

As the CBM and VBM potentials of g-C_3N_4 are 1.19 and 0.3 eV lower than that of H^+/H_2, respectively, they indicate that g-C_3N_4 has enough oxidation and reduction potentials to act on water. According to the Fermi level changes, the relative positions of the CB and VB of g-C_3N_4 and BiOBr(001) change after contact. For g-C_3N_4, the CBM potential (−1.58 eV) is lower and the VBM potential (2.05 eV) is higher than the values before the heterojunction is formed. According to these results, g-C_3N_4 in the heterojunction is more active for the hydrogen evolution reaction and the OER. BiOBr(001) has a CBM potential of 0.16 eV, which is not lower than the reduction potential of H^+/H_2. Compared with the oxidation potential of H_2O and O_2/H_2O, the VBM potential is higher (2.76 eV), indicating a high activity level for OERs. In contrast to the isolated g-C_3N_4 and BiOBr(001), however, the VBM and CBM values of C_3N_4 after the heterojunction is formed is slightly lower than those before. The g-C_3N_4/BiOBr(001) heterojunction is more suitable for photocatalytic water splitting.

3.2. Effect of an External Electric Field. The external electric field (E-field) is commonly used to modulate the electronic behavior.[57] In order to investigate this, the effect of the electric field is considered here. An electric field is applied vertically, and the positive direction of the electric field is defined as the direction from g-C_3N_4 to BiOBr(001). We chose to use E-fields that ranged from −0.7 to +0.9 V/Å, with a 0.02 V/Å interval between them. Figure 7a shows how the

https://doi.org/10.1021/acsomega.2c04298
ACS Omega 2022, 7, 36479−36488

band gap of the heterostructure varies as a function of the electric field (E_{ext}). It indicates that the band gap does not vary monotonically with E_{ext}. For $0 < E_{ext} < 0.5$ V/Å, the band gap increases as E_{ext} increases. However, for$E_{ext} > 0.5$ V/Å, the band gap linearly decreases with E_{ext} increasing. When E_{ext} is set equal to 0.5 V/Å, the g-C_3N_4/BiOBr(001) heterostructure has the maximum band gap of approximately 2.6 eV. Whenever the negative external electric field is applied, the band gap decreases as the electric field's strength increases. Therefore, the presence of an electric field can modulate the band gap of g-C_3N_4/BiOBr(001).

Figure 7b illustrates the effect of the applied electric field on the band gap of g-C_3N_4/BiOBr(001) and the CBM and VBM of g-C_3N_4 and BiOBr(001). They are obtained from the PDOS of g-C_3N_4 and BiOBr(001) in g-C_3N_4/BiOBr(001) under the influence of an electric field (Figure 8). The obtained results

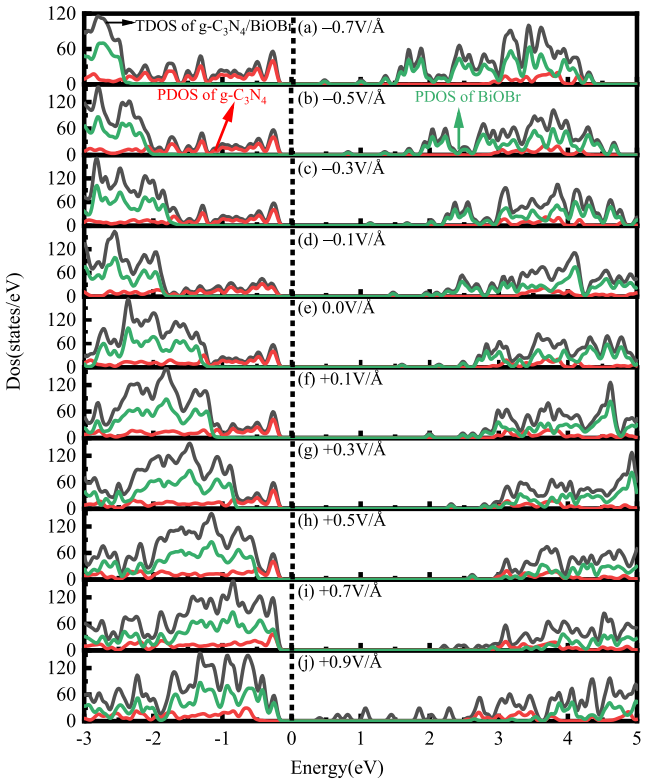

Figure 8. TDOS of g-C_3N_4/BiOBr(001) and PDOS of g-C_3N_4 and BiOBr(001) in g-C_3N_4/BiOBr(001) under applied electric fields of (a) 0.7, (b) 0.5, (c) 0.3, (d) 0.1, (e) 0, (f) +0.1, (g) +0.3, (h) +0.5, (i) +0.7, and (j) +0.9 V/Å.

clearly show that the type II energy band arrangement of the g-C_3N_4/BiOBr(001) vdW heterojunction is maintained under the applied electric field (except for 0.7 and 0.9 V/Å). It was shown that the g-C_3N_4 VBM was not affected by the applied electric field and remained at −0.16 eV, whereas the g-C_3N_4 CBM remained relatively unchanged. In contrast, the BiOBr(001) CBM and BiOBr(001) VBM energies shifted monotonically upward. Thus, the VBM of the two materials' crossing points appear at $E_{ext} = 0.7$ V/Å. As a result, this can be attributed to the change in the local electrostatic potential energy difference between the two layers that occurs directly due to the electric field. Thus, when the applied electric field is $-0.7 \leq E \leq 0.9$ V/Å, the BiOBr(001) layer contributes to the VBM of heterostructures, unlike the g-C_3N_4 layer, which contributes to the CBM.

In the case that the vertical electric field $E > 0.5$ V/Å, the CBM of g-C_3N_4 is still a bit higher than the CBM of BiOBr(001), and the VBM of BiOBr(001) gradually increases above the VBM of g-C_3N_4. For the time being, the heterostructure consists of the type I band alignment. According to Figure 8, the TDOS and PDOS of g-C_3N_4 and BiOBr(001) in external electric fields are indicated. As a result, it can be seen that the relationship between the band gap of g-C_3N_4/BiOBr(001) and the external electric field reveals that the direction and magnitude of the electric field play a significant role in the electron transport of the heterostructure. These results are beneficial for the development of future photocatalysis technology.

From the frequency-dependent complex dielectric function of the g-C_3N_4 monolayer, the BiOBr(001) surface, and g-C_3N_4/BiOBr(001), the absorption coefficients can be obtained.[58−60] However, more GW ("G" is the one-body Green's function, which describes the propagation of a particle in an interacting system, and "W" is the linear response dynamically screened Coulomb interaction) and BSE[61] (Bethe−Salpeter equation) calculations for the g-C_3N_4 monolayer, the BiOBr(001) surface, and g-C_3N_4/BiOBr(001) are limited by their expensive computational time in this paper, which agrees with the previous study[62] (Note S3). Figure 9a shows frequency-dependent absorption coefficients for g-C_3N_4 monolayers, BiOBr(001) surfaces, and g-C_3N_4/BiOBr(001). They range between 0 and 3.6 eV when calculated using the HSE method in the [001] direction. An isolated g-C_3N_4 sheet exhibits clear absorption above 2.7 eV, as was observed in a previous study.[63] In the case of BiOBr(001), the absorption edge has been calculated to have a value of approximately 2.3 eV. It appears that the g-C_3N_4/BiOBr(001) heterojunction absorbance is significantly improved compared to that of g-C_3N_4 and BiOBr(001), with an absorption edge of approximately 2.15 eV. This enhanced performance is possible because electrons are directly excited from the CB of the g-C_3N_4 layer to the VB of the BiOBr(001) sheet. These results are consistent with the electronic properties above and previous experiments.[64]

In this study, we calculated the variation of the absorption coefficient $\alpha(\omega)$ of g-C_3N_4/BiOBr(001) along the z-direction for different electric field strengths (−0.7, −0.5, −0.3, −0.1, 0, +0.1, +0.3, +0.5, +0.7, and +0.9 V/Å), which is shown in Figure 9b. According to the results, the optical absorption in the z-direction exhibits strong light absorption in the visible light region and is highly sensitive to the electric field. When the electric field is −0.7, −0.5, −0.3, −0.1, and +0.5 V/Å, compared with the optical absorption of the heterostructure without an electric field, we found a significant red shift at the absorption edge. Nevertheless, the absorption edge is blue-shifted when the electric field is +0.1, +0.3, +0.7, and +0.9 V/Å. Under an electric field, the peak of light absorption is significantly enhanced in the visible light region. Our results suggest that g-C_3N_4/BiOBr(001) can be improved optically by applying an electric field.

4. CONCLUSIONS

Here, we theoretically investigated the geometric structure, electronic structure, and photocatalytic properties of g-C_3N_4/BiOBr(001) by HSE hybrid DFT calculations. We demonstrated that g-C_3N_4/BiOBr could function as a type-II

https://doi.org/10.1021/acsomega.2c04298
ACS Omega 2022, 7, 36479−36488

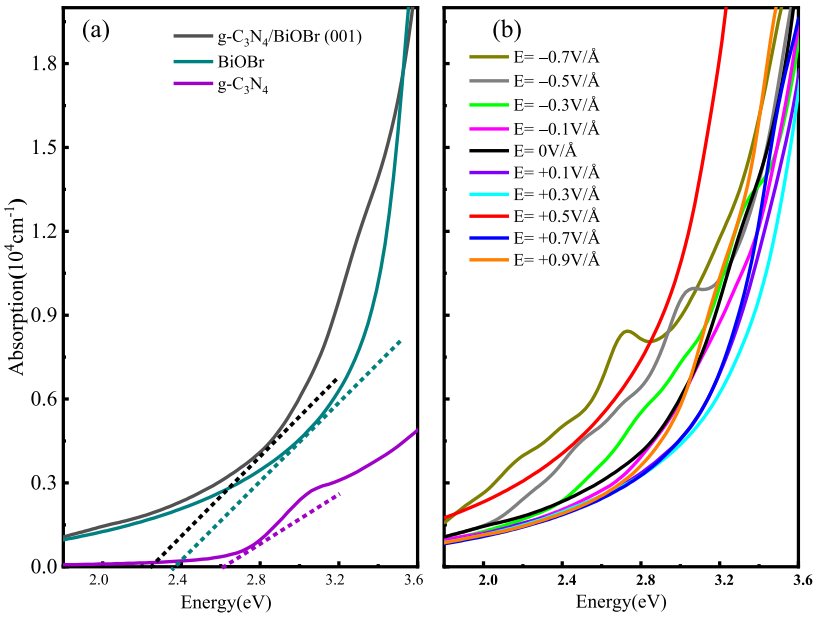

Figure 9. (a) Calculated absorption coefficients for g-C_3N_4, BiOBr(001), and g-C_3N_4/BiOBr(001) using the HSE06 method. (b) Absorption coefficients for g-C_3N_4/BiOBr(001) under E-field values of −0.7, −0.5, −0.3, −0.1, 0, +0.1, +0.3, +0.5, +0.7, and +0.9 V/Å.

heterojunction. This heterojunction allows the electrons and holes to be separated at the interface. Moreover, we find that the electronic structure and band alignment of g-C_3N_4/BiOBr(001) can be tuned using external electric fields. It is also noteworthy that the optical absorption peak in the visible region is enhanced under the action of the electric field. The electric field may even improve the optical properties of the g-C_3N_4/BiOBr(001) heterostructure. These theoretical studies may provide new insights into the potential enhancement mechanism of the photocatalytic activity of g-C_3N_4/BiOBr-(001).

■ ASSOCIATED CONTENT

Supporting Information

The Supporting Information is available free of charge at https://pubs.acs.org/doi/10.1021/acsomega.2c04298.

Slab models of 2Br-terminated, 1Br-terminated, and BiO-terminated BiOBr (001) surfaces; schematic illustration for the accessible chemical potential range; the calculated surface energies (J/m^2) for various atomic termination surfaces BiOBr (001); and variations of temperature and energy plotted as a function of time for AIMD simulations of g-C_3N_4/BiOBr(001) (PDF)

■ AUTHOR INFORMATION

Corresponding Author

Wentao Wang − *College of Physics and Electronic Science, Guizhou Normal University, Guiyang 550025, China; Guizhou Provincial Key Laboratory of Computational Nano-Material Science, Guizhou Education University, Guiyang 550018, China;* orcid.org/0000-0003-4308-3515; Email: wuli8@163.com

Authors

Wenzhi Yao − *Department of Environmental and Municipal Engineering, North China University of Water Conservancy and Electric Power, Zhengzhou 450011, China*

Dongying Li − *Department of Environmental and Municipal Engineering, North China University of Water Conservancy and Electric Power, Zhengzhou 450011, China*

Shuai Wei − *Department of Environmental and Municipal Engineering, North China University of Water Conservancy and Electric Power, Zhengzhou 450011, China*

Xiaoqing Liu − *Department of Environmental and Municipal Engineering, North China University of Water Conservancy and Electric Power, Zhengzhou 450011, China*

Xuefei Liu − *College of Physics and Electronic Science, Guizhou Normal University, Guiyang 550025, China;* orcid.org/0000-0003-0154-474X

Complete contact information is available at: https://pubs.acs.org/10.1021/acsomega.2c04298

Notes

The authors declare no competing financial interest.

■ ACKNOWLEDGMENTS

W.Y. thanks Professor Weizhong Han for valuable discussions. This work was supported by the National Natural Science Foundation of China (Grant no. 52262031); the training program for young backbone teachers in Colleges and universities in Henan Province (2021GGJS079); the training of young backbone teachers at the school level of North China University of Water Resources and Electric Power (2020010); the 2021 Henan Provincial undergraduate innovation and entrepreneurship training program (S202110078013), the High-level talent project (40732), and the North China University of Water Resources and Electric Power Master's Innovation Ability Improvement Project (YK-2021-86). This work was carried out at the Shanxi Supercomputing Center of China, and the calculations were performed on TianHe-2. The authors also thank the Supercomputing Center of the USTC for providing the computational time.

REFERENCES

(1) Zhang, J.; Zhang, M.; Sun, R. Q.; Wang, X. A Facile Band Alignment of Polymeric Carbon Nitride Semiconductors to Construct Isotype Heterojunctions. *Angew. Chem.* **2012**, *51*, 10145−10149.

(2) Li, J.; Zhao, K.; Yu, Y.; Zhang, L. Facet-Level Mechanistic Insights into General Homogeneous Carbon Doping for Enhanced Solar-to-Hydrogen Conversion. *Adv. Funct. Mater.* **2015**, *25*, 2189−2201.

(3) Venkata Reddy, C.; Neelakanta Reddy, I.; Ravindranadh, K.; Raghava Reddy, K.; Shim, J.; Cheolho, B. Au-Doped $BiVO_4$ Nanostructure-Based Photoanode with Enhanced Photoelectrochemical Solar Water Splitting and Electrochemical Energy Storage Ability. *Appl. Surf. Sci.* **2021**, *545*, 149030.

(4) Wang, G.; Chang, J.; Tang, W.; Xie, W.; Ang, Y. S. 2D Materials and Heterostructures for Photocatalytic Water-Splitting: A Theoretical Perspective. *J. Phys. D: Appl. Phys.* **2022**, *55*, 293002.

(5) Wang, G.; Tang, W.; Xie, W.; Tang, Q.; Wang, Y.; Guo, H.; Gao, P.; Dang, S.; Chang, J. Type-II Cds/Ptsse Heterostructures Used as Highly Efficient Water-Splitting Photocatalysts. *Appl. Surf. Sci.* **2022**, *589*, 152931.

(6) Guo, W.; Feng, Q.; Tao, Y.; Zheng, L.; Han, Z.; Ma, J. Systematic Investigation on the Gas-Sensing Performance of TiO_2 Nanoplate Sensors for Enhanced Detection on Toxic Gases. *Mater. Res. Bull.* **2016**, *73*, 302−307.

(7) Cheng, C.; Fang, W.-H.; Long, R.; Prezhdo, O. V. Water Splitting with a Single-Atom Cu/TiO_2 Photocatalyst: Atomistic Origin of High Efficiency and Proposed Enhancement by Spin Selection. *JACS Au* **2021**, *1*, 550−559.

(8) Goktas, S.; Goktas, A. A Comparative Study on Recent Progress in Efficient ZnO Based Nanocomposite and Heterojunction Photocatalysts: A Review. *J. Alloys Compd.* **2021**, *863*, 158734.

(9) Wei, Y.; Wan, J.; Wang, J.; Zhang, X.; Yu, R.; Yang, N.; Wang, D. Hollow Multishelled Structured $SrTiO_3$ with La/Rh Co-Doping for Enhanced Photocatalytic Water Splitting under Visible Light. *Small* **2021**, *17*, No. e2005345.

(10) Abid, A. Y.; Sun, Y.; Hou, X.; Tan, C.; Zhong, X.; Zhu, R.; Chen, H.; Qu, K.; Li, Y.; Wu, M.; Zhang, J.; Wang, J.; Liu, K.; Bai, X.; Yu, D.; Ouyang, X.; Wang, J.; Li, J.; Gao, P. Creating Polar Antivortex in $Pbtio_3/SrTiO_3$ Superlattice. *Nat. Commun.* **2021**, *12*, 2054.

(11) Zhang, X.; Li, T.; Guan, M.; Li, R.; Liu, J.; Wang, Y.; Zhang, C.; Fan, C. DFT Insights into the Migration of Effective Electrons Towards O_2 for OH Formation over Electron-Rich Sites on BiOBr (0 0 1) Surface. *Appl. Surf. Sci.* **2021**, *567*, 150828.

(12) Wang, X.; Zhang, Y.; Mei, H.; Xu, H.; Gan, L.; Zhang, R. Meso-Erythritol-Regulated BiOBr Nanosheets with Surface Hydroxyl Imprinting Sites for Considerably Improved Photocatalytic Capability. *Appl. Surf. Sci.* **2021**, *546*, 149116.

(13) Shao, L.; Liu, Y.; Wang, L.; Xia, X.; Shen, X. Electronic Structure Tailoring of BiOBr (0 1 0) Nanosheets by Cobalt Doping for Enhanced Visible-Light Photocatalytic Activity. *Appl. Surf. Sci.* **2020**, *502*, 143895.

(14) Obeid, M. M.; Stampfl, C.; Bafekry, A.; Guan, Z.; Jappor, H. R.; Nguyen, C. V.; Naseri, M.; Hoat, D. M.; Hieu, N. N.; Krauklis, A. E.; Vu, T. V.; Gogova, D. First-Principles Investigation of Nonmetal Doped Single-Layer BiOBr as a Potential Photocatalyst with a Low Recombination Rate. *Phys. Chem. Chem. Phys.* **2020**, *22*, 15354−15364.

(15) Imam, S. S.; Adnan, R.; Mohd Kaus, N. H. The Photocatalytic Potential of BiOBr for Wastewater Treatment: A Mini-Review. *J. Environ. Chem. Eng.* **2021**, *9*, 105404.

(16) Shi, M.; Li, G.; Li, J.; Jin, X.; Tao, X.; Zeng, B.; Pidko, E. A.; Li, R.; Li, C. Intrinsic Facet-Dependent Reactivity of Well-Defined BiOBr Nanosheets on Photocatalytic Water Splitting. *Angew. Chem.* **2020**, *59*, 6590−6595.

(17) Hu, T.; Yang, Y.; Dai, K.; Zhang, J.; Liang, C. A Novel Z-Scheme Bi_2MoO_6/BiOBr Photocatalyst for Enhanced Photocatalytic Activity under Visible Light Irradiation. *Appl. Surf. Sci.* **2018**, *456*, 473−481.

(18) Wang, G.; Luo, X.; Huang, Y.; Kuang, A.; Yuan, H.; Chen, H. BiOX/Bioy (X, Y = F, Cl, Br, I) Superlattices for Visible Light Photocatalysis Applications. *RSC Adv.* **2016**, *6*, 91508−91516.

(19) Cao, X.; Shi, J.-j.; Zhang, M.; Jiang, X.-h.; Zhong, H.-x.; Huang, P.; Ding, Y.-m.; Wu, M. Band Gap Opening of Graphene by Forming Heterojunctions with the 2D Carbonitrides Nitrogenated Holey Graphene, $g\text{-}C_3N_4$, and G-Cn: Electric Field Effect. *J. Phys. Chem. C* **2016**, *120*, 11299−11305.

(20) Mitra, A.; Howli, P.; Sen, D.; Das, B.; Chattopadhyay, K. K. $Cu_2O/g\text{-}C_3N_4$ Nanocomposites: An Insight into the Band Structure Tuning and Catalytic Efficiencies. *Nanoscale* **2016**, *8*, 19099−19109.

(21) Xue, Z.; Zhang, X.; Qin, J.; Liu, R. Constructing $MoS_2/g\text{-}C_3N_4$ Heterojunction with Enhanced Oxygen Evolution Reaction Activity: A Theoretical Insight. *Appl. Surf. Sci.* **2020**, *510*, 145489.

(22) Wang, B.; Wang, G.; Yuan, H.; Kuang, A.; Chang, J.; Huang, Y.; Chen, H. Strain-Tunable Electronic and Optical Properties in Two Dimensional $GaSe/g\text{-}C_3N_4$ Van Der Waals Heterojunction as Photocatalyst for Water Splitting. *Phys. E* **2020**, *118*, 113896.

(23) Ma, T.; Shen, Q.; Xue, B. Z. J.; Guan, R.; Liu, X.; Jia, H.; Xu, B. Facile Synthesis of Fe-Doped $g\text{-}C_3N_4$ for Enhanced Visible-Light Photocatalytic Activity. *Inorg. Chem. Commun.* **2019**, *107*, 107451.

(24) He, C.; Zhang, J. H.; Zhang, W. X.; Li, T. T. Type-II Inse/ $g\text{-}C_3N_4$ Heterostructure as a High-Efficiency Oxygen Evolution Reaction Catalyst for Photoelectrochemical Water Splitting. *J. Phys. Chem. Lett.* **2019**, *10*, 3122−3128.

(25) Wang, Z.; Huang, Y.; Ho, W.; Cao, J.; Shen, Z.; Lee, S. C. Fabrication of $Bi_2O_2CO_3/g\text{-}C_3N_4$ Heterojunctions for Efficiently Photocatalytic No in Air Removal: In-Situ Self-Sacrificial Synthesis, Characterizations and Mechanistic Study. *Appl. Catal., B* **2016**, *199*, 123−133.

(26) Tang, L.; Feng, C.; Deng, Y.; Zeng, G.; Wang, J.; Liu, Y.; Feng, H.; Wang, J. Enhanced Photocatalytic Activity of Ternary Ag/$g\text{-}C_3N_4/NaTaO_3$ Photocatalysts under Wide Spectrum Light Radiation: The High Potential Band Protection Mechanism. *Appl. Catal., B* **2018**, *230*, 102−114.

(27) Tian, N.; Huang, H.; Guo, Y.; He, Y.; Zhang, Y. A $g\text{-}C_3N_4/Bi_2O_2CO_3$ Composite with High Visible-Light-Driven Photocatalytic Activity for Rhodamine B Degradation. *Appl. Surf. Sci.* **2014**, *322*, 249−254.

(28) Song, T.; Yu, X.; Tian, N.; Huang, H.-w. Preparation, Structure and Application of $g\text{-}C_3N_4$/BiOX Composite Photocatalyst. *Int. J. Hydrogen Energy* **2021**, *46*, 1857−1878.

(29) Liang, Y.; Zeng, Z.; Yang, J.; Yang, G.; Han, Y. Designing Heterointerface in $BiOBr/g\text{-}C_3N_4$ Photocatalyst to Enhance Visible-Light-Driven Photocatalytic Performance in Water Purification. *Colloids Surf., A* **2021**, *624*, 126796.

(30) Li, H.; Ma, A.; Zhang, D.; Gao, Y.; Dong, Y. Rational Design Direct Z-Scheme $BiOBr/g\text{-}C_3N_4$ Heterojunction with Enhanced Visible Photocatalytic Activity for Organic Pollutants Elimination. *RSC Adv.* **2020**, *10*, 4681−4689.

(31) Zhang, B.; Hu, X.; Liu, E.; Fan, J. Novel S-Scheme 2D/2D $BiOBr/g\text{-}C_3N_4$ Heterojunctions with Enhanced Photocatalytic Activity. *Chin. J. Catal.* **2021**, *42*, 1519−1529.

(32) Vinoth, S.; Pandikumar, A. Ni Integrated $S\text{-}g\text{-}C_3N_4$/BiOBr Based Type-II Heterojunction as a Durable Catalyst for Photoelectrochemical Water Splitting. *Renewable Energy* **2021**, *173*, 507−519.

(33) Ye, L.; Liu, J.; Jiang, Z.; Peng, T.; Zan, L. Facets Coupling of BiOBr-g-C3N4 Composite Photocatalyst for Enhanced Visible-Light-Driven Photocatalytic Activity. *Appl. Catal., B* **2013**, *142*−*143*, 1−7.

(34) Huang, L.; Liu, J.; Li, P.; Li, Y.; Wang, C.; Shu, S.; Song, Y. Cqds Modulating Z-Scheme $g\text{-}C_3N_4$/BiOBr Heterostructure for Photocatalytic Removing Rhb, Bpa and Tc and E. Coli by Led Light. *J. Alloys Compd.* **2022**, *895*, 162637.

(35) Yan, M.-Y.; Jiang, Z.-Y.; Zheng, J.-M.; Lin, Y.-M.; Zhang, Z.-Y. Theoretical Study on Transport-Scheme Conversion of $g\text{-}C_3N_4/TiO_2$ Heterojunctions by Oxygen Vacancies. *Appl. Surf. Sci.* **2020**, *531*, 147318.

https://doi.org/10.1021/acsomega.2c04298
ACS Omega 2022, 7, 36479−36488

(36) Kresse, G.; Furthmüller, J. Efficiency of Ab-Initio Total Energy Calculations for Metals and Semiconductors Using a Plane-Wave Basis Set. *Comp. Mater. Sci.* **1996**, *6*, 15−50.
(37) Kresse, G.; Furthmüller, J. Efficient Iterative Schemes for Ab Initio Total-Energy Calculations Using a Plane-Wave Basis Set. *Phys. Rev. B: Condens. Matter Mater. Phys.* **1996**, *54*, 11169.
(38) Blöchl, P. E. Projector Augmented-Wave Method. *Phys. Rev. B* **1994**, *50*, 17953−17979.
(39) Perdew, J. P.; Burke, K.; Ernzerhof, M. Generalized Gradient Approximation Made Simple. *Phys. Rev. Lett.* **1996**, *77*, 3865.
(40) Perdew, J. P.; Wang, Y. Accurate and Simple Analytic Representation of the Electron-Gas Correlation Energy. *Phys. Rev. B: Condens. Matter Mater. Phys.* **1992**, *45*, 13244−13249.
(41) Heyd, J.; Scuseria, G. E.; Ernzerhof, M. Hybrid Functionals Based on a Screened Coulomb Potential. *J. Chem. Phys.* **2003**, *118*, 8207−8215.
(42) Grimme, S.; Ehrlich, S.; Goerigk, L. Effect of the Damping Function in Dispersion Corrected Density Functional Theory. *J. Comput. Chem.* **2011**, *32*, 1456−1465.
(43) Neugebauer, J.; Scheffler, M. Adsorbate-Substrate and Adsorbate-Adsorbate Interactions of Na and K Adlayers on Al(111). *Phys. Rev. B: Condens. Matter Mater. Phys.* **1992**, *46*, 16067−16080.
(44) Nosé, S. A Unified Formulation of the Constant Temperature Molecular Dynamics Methods. *J. Chem. Phys.* **1984**, *81*, 511−519.
(45) Zhang, J.; Ren, F.; Deng, M.; Wang, Y. Enhanced Visible-Light Photocatalytic Activity of a g-C_3N_4/$BiVO_4$ Nanocomposite: A First-Principles Study. *Phys. Chem. Chem. Phys.* **2015**, *17*, 10218−10226.
(46) Teshome, T.; Datta, A. Two-Dimensional Graphene-Gold Interfaces Serve as Robust Templates for Dielectric Capacitors. *ACS Appl. Mater. Interfaces* **2017**, *9*, 34213−34220.
(47) Mukherjee, M.; Jana, R.; Datta, A. Designing C6n6/C2N Van Der Waals Heterostructures for Photogenerated Charge Carrier Separation. *Phys. Chem. Chem. Phys.* **2021**, *23*, 3925−3933.
(48) Du, Y.; Liu, H.; Hu, J.; Deng, L.; Bai, Y.; Bai, M.; Xie, F. First-Principles Study of the Electronic and Optical Properties of Bi_2se_3/$MoSe_2$ Heterojunction. *Phys. Status Solidi B* **2021**, *258*, 2100403.
(49) Tang, W.; Sanville, E.; Henkelman, G. A Grid-Based Bader Analysis Algorithm without Lattice Bias. *J. Phys.: Condens. Matter* **2009**, *21*, 084204.
(50) Chen, Y.; Shi, T.; Liu, P.; Ma, X.; Shui, L.; Shang, C.; Chen, Z.; Wang, X.; Kempa, K.; Zhou, G. Insights into the Mechanism of Enhanced Visible-Light Photocatalytic Activity of Black Phosphorus/$BiVO_4$ Heterostructure: A First-Principles Study. *J. Mater. Chem. A* **2018**, *6*, 19167−19175.
(51) Liu, J. Origin of High Photocatalytic Efficiency in Monolayer g-C_3N_4/Cds Heterostructure: A Hybrid DFT Study. *J. Phys. Chem. C* **2015**, *119*, 28417−28423.
(52) Gao, B.; Zhang, J.-R.; Chen, L.; Guo, J.; Shen, S.; Au, C.-T.; Yin, S.-F.; Cai, M.-Q. Density Functional Theory Calculation on Two-Dimensional MoS_2/BiOX (X = Cl, Br, I) Van Der Waals Heterostructures for Photocatalytic Action. *Appl. Surf. Sci.* **2019**, *492*, 157−165.
(53) Dai, K.; Lu, L.; Liang, C.; Zhu, G.; Liu, Q.; Geng, L.; He, J. A High Efficient Graphitic-C_3N_4/BiOI/Graphene Oxide Ternary Nanocomposite Heterostructured Photocatalyst with Graphene Oxide as Electron Transport Buffer. *Dalton Trans.* **2015**, *44*, 7903−7910.
(54) Chang, F.; Li, C.; Chen, J.; Wang, J.; Luo, P.; Xie, Y.; Deng, B.; Hu, X. Enhanced Photocatalytic Performance of g-C_3N_4 Nanosheets-BiOBr Hybrids. *Superlattices Microstruct.* **2014**, *76*, 90−104.
(55) Cao, S.; Yu, J. g-C_3N_4-Based Photocatalysts for Hydrogen Generation. *J. Phys. Chem. Lett.* **2014**, *5*, 2101−2107.
(56) Reza Gholipour, M.; Dinh, C. T.; Béland, F.; Do, T. O. Nanocomposite Heterojunctions as Sunlight-Driven Photocatalysts for Hydrogen Production from Water Splitting. *Nanoscale* **2015**, *7*, 8187−8208.
(57) Chen, X.; Tan, C.; Yang, Q.; Meng, R.; Liang, Q.; Jiang, J.; Sun, X.; Yang, D. Q.; Ren, T. Effect of Multilayer Structure, Stacking Order and External Electric Field on the Electrical Properties of Few-Layer Boron-Phosphide. *Phys. Chem. Chem. Phys.* **2016**, *18*, 16229−16236.
(58) Zhang, J.; Cao, J. X.; Chen, X.; Ding, J. W.; Zhang, P.; Ren, W. Diamond Nanowires with Nitrogen Vacancy under a Transverse Electric Field. *Phys. Rev. B: Condens. Matter Mater. Phys.* **2015**, *91*, 045417.
(59) Saha, S.; Sinha, T.; Mookerjee, A. Electronic Structure, Chemical Bonding, and Optical Properties of Paraelectric BaTiO3. *Phys. Rev. B: Condens. Matter Mater. Phys.* **2000**, *62*, 8828−8834.
(60) Zhang, J.; Deng, M.; Yan, Y.; Xiao, T.; Ren, W.; Zhang, P. Tunable Type-II $BiVO_4$/g-C_3N_4 Nanoheterostructures for Photocatalysis Applications. *Phys. Rev. Appl.* **2019**, *11*, 044052.
(61) Onida, G.; Reining, L.; Rubio, A. Electronic Excitations: Density-Functional Versus Many-Body Green's-Function Approaches. *Rev. Mod. Phys.* **2002**, *74*, 601−659.
(62) Zhang, J.; Deng, P.; Deng, M.; Shen, H.; Feng, Z.; Li, H. Hybrid Density Functional Theory Study of Native Defects and Nonmetal (C, N, S, and P) Doping in a Bi_2WO_6 Photocatalyst. *ACS Omega* **2020**, *5*, 29081−29091.
(63) Wang, J.; Guan, Z.; Huang, J.; Li, Q.; Yang, J. Enhanced Photocatalytic Mechanism for the Hybrid g-C_3N_4/MoS_2 Nanocomposite. *J. Mater. Chem. A* **2014**, *2*, 7960−7966.
(64) Sun, J.; Song, J.; Gondal, M. A.; Shi, S.; Lu, Z.; Xu, Q.; Chang, X.; Xiang, D.; Shen, K. Preparation of g-C_3N_4/BiOX (X = Cl, Br, I) Composites, and Their Photocatalytic Activity under Visible Light Irradiation. *Res. Chem. Intermed.* **2015**, *41*, 6941−6955.

https://doi.org/10.1021/acsomega.2c04298
ACS Omega 2022, 7, 36479−36488